

3-center-3-electron σ -Adduct Enables Silyl Radical Transfer Below the Minimum Barrier for Silyl Radical Formation

Zihang Qiu^{1#}, Paolo Cleto Bruzzese^{2#}, Zikuan Wang^{1#}, Hao Deng^{1#}, Markus Leutzsch¹, Christophe Farès¹, Sonia Chabbra^{2†}, Frank Neese¹, Alexander Schnegg^{2*}, and Constanze N. Neumann^{1*}

¹Max-Planck-Institut für Kohlenforschung, Kaiser-Wilhelm-Platz 1, 45470, Mülheim an der Ruhr, Germany.

²Max-Planck-Institut für Chemische Energiekonversion, Stiftstrasse 34-36, 45470, Mülheim an der Ruhr, Germany.

KEYWORDS Rh(II) metalloradicals, MOF site-isolation, hydrosilylation catalysis, MOF catalysis, 3-center-3-electron interaction

ABSTRACT: Transition-metal-catalyzed cleavage of the Si–H bond in silanes to yield silyl radicals requires substantial amounts of energy, which is commonly supplied by photons. For Rh(II) porphyrins, efficient hydrosilylation catalysis only becomes accessible upon site isolation in a MOF, and the formation of free silyl radicals likewise requires irradiation. Within the MOF, however, an uncommonly facile direct silyl radical transfer to olefin substrates is also possible, which makes thermal olefin hydrosilylation accessible at room temperature. The ability of MOF-supported Rh(II) metalloradicals to furnish an unprecedented 3-center-3-electron (3c-3e) Rh(II)-silane σ -adduct enables the assembly of a tri-component transition state that is comprised of Rh(II), silane and ethylene. The tri-component transition state bypasses the high-energy silyl radical species and enables silyl radical transfer with an activation free energy ~ 15 kcal·mol⁻¹ below the minimum energy barrier for silyl radical formation. We report direct observation of the 3c-3e silane σ -adduct, which is a stable species in the absence of light and olefins. Furthermore, a combination of experiments and quantum mechanical calculations show that direct silyl radical transfer to ethylene is promoted by the temporary oxidation of the transition structure by a proximal Rh(II) center. Thus, the crucial role of the MOF matrix is to fix the inter-Rh separation in our catalyst at a value large enough for 3c-3e silane adduct formation, but short enough for facile electron transfer.

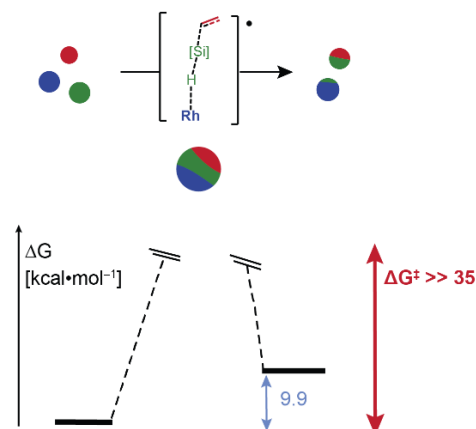
INTRODUCTION

Photons are a necessary component of a rapidly increasing number of synthetic transformations.¹ In the majority of cases, illumination is used to generate high-energy open shell intermediates, which can engage in subsequent reaction steps with small kinetic barriers. The development of photocatalysts that permit the use of visible rather than UV light to cleave strong bonds vastly increased the scope and practical utility of photochemical reactions.² Even visible light photons are highly energetic, however, with 450 nm photons carrying an energy of 63.6 kcal·mol⁻¹. Since many synthetic reactions have low quantum yields, the high reactivity of radical intermediates comes at a substantial energy cost. Ideally, we could harness the versatile reactivity of high-energy radicals without ever having to generate them as free species. An energy-efficient direct transfer of an incipient radical to a radical acceptor could unlock more energy efficient and sustainable radical reactions. For a reaction involving a catalyst, a radical generator and a radical acceptor species, a direct transfer reaction would be possible if all three species could be assembled together. But except under extreme conditions, such as those present during the formation of a star, triatomic collisions rarely take place.³ An additional challenge is that the catalyst and both reagents are not atoms, but molecules of reasonable complexity. For multi-atomic molecules, not only the minute collision frequency but also the need for correct alignment

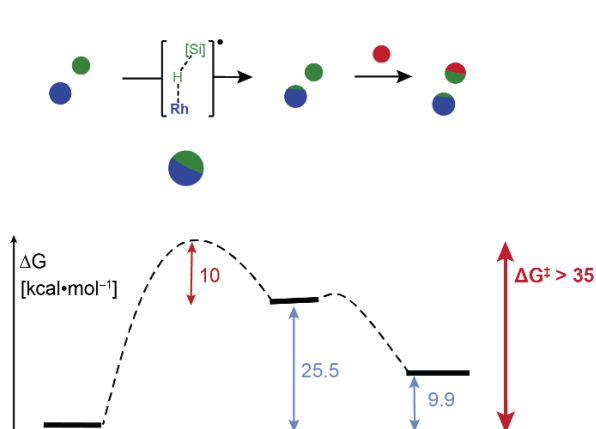
of all species renders it unlikely for termolecular steps to contribute noticeably to reaction rates (Figure 1A). Terrestrial chemical transformations thus generally proceed via successive uni- and bi-molecular reaction steps.^{4, 5} In the case of catalytic radical hydrosilylation reaction, an initial encounter between catalyst and silane leads to the formation of a free silyl radical, which then reacts with an olefin in a separate reaction step (Figure 1B). For Rh(II) porphyrin catalysis, the difference in Gibbs free energy between the reagents (silane and Rh(II)) and the products (Rh(III)-H and silyl radical) is calculated to be 25.5 kcal·mol⁻¹ (Figure S69). However, for hydrogen atom transfer (HAT) to take place, two molecules need to associate into a transition structure which results in energy penalty due to the loss of translational and rotational degrees of freedom that corresponds to approximately 10 kcal·mol⁻¹.⁶⁻⁸ A catalyst that is able to assemble a silane and an olefin into a transition state for direct radical transfer with an energy input of less than 25.5 + 10 = 35.5 kcal·mol⁻¹ would thus permit a more energy-efficient transformation. Such a transition state would need to be assembled in a step-wise fashion to limit the entropic penalty. We define here the term “tri-component” as a transition state that brings together three individual species but is not assembled via a termolecular collision, and thus entropically accessible (Figure 1C). To render the formation of a tri-component transition state feasible,

the Rh(II) catalyst and the silane need to be able to form an adduct with sufficient stability that it survives under the reaction conditions for an appreciable amount of time.

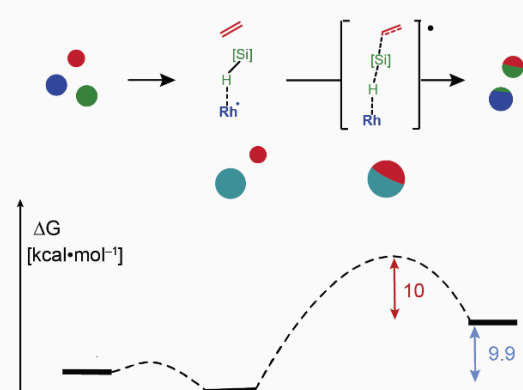
A Trimolecular Transition State



B Free Radical Pathway



C Design: Tri-Component Transition State



D Result: Low-Barrier Radical Transfer

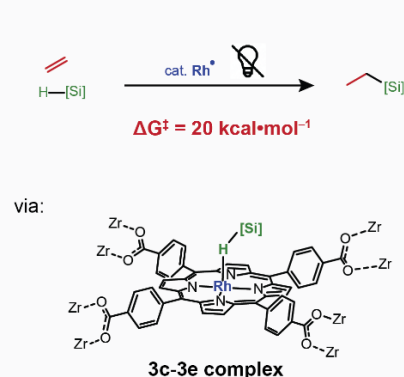


Figure 1. A) Direct transfer of a silyl radical equivalent to an acceptor is associated with a prohibitively high entropic barrier, so that radical hydrosilylation instead proceeds in a step-wise manner via the intermediacy of free silyl radicals (B). If a 3c-3e σ -adduct between the catalyst and silane could be accessed, direct silyl radical transfer would be rendered entropically feasible (C). (D) A MOF-based Rh(II) catalyst that can stabilize a 3c-3e adduct is able to promote thermal hydrosilylation with a barrier of $\Delta G^\ddagger = 20$ kcal·mol⁻¹. Spheres represent individual molecules that are present. Small red arrows indicate the anticipated entropy contribution to the minimum energy pathway; large red arrows depict the total energy associated with the minimum energy pathway.

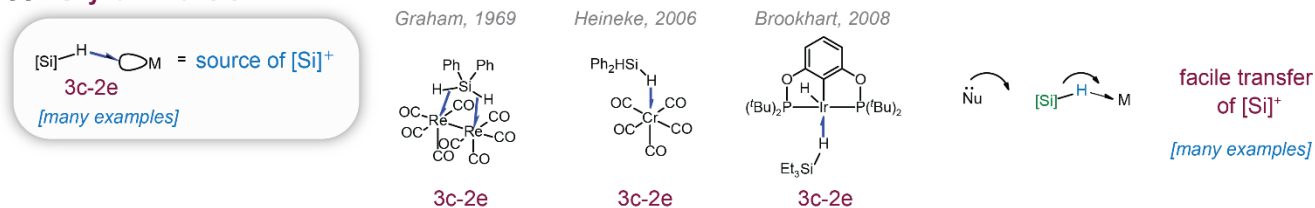
Existing examples in which the assembly of silanes and substrates by a transition metal center leads to transformations with a low activation barrier can be found for the formal transfer of silylium cations (Figure 2A). A mechanism put forth originally by Crabtree, and extensively refined by Brookhart and Oestreich invokes a 3-center-2-electron (3c-2e) interaction between a silane and an empty transition metal orbital as a crucial reaction intermediate.⁹⁻¹² Binding of the silane to the metal center enables a low energy barrier transfer of a silylium equivalent to polar substrates such as ketones,^{12, 13} alcohols,¹⁴ CO₂,^{15, 16} and even weakly nucleophilic alkyl halides and dialkylethers.¹⁷⁻¹⁹ Inspired by the role of the 3c-2e interaction in providing a low energy pathway for the formal transfer of silylium, we aimed to access a corresponding 3c-3e silane σ -adduct to facilitate silyl radical transfer (Figure 2B). While many metal complexes

featuring 3c-2e silane adducts have been studied and structurally characterized,^{14, 20-24} to the best of our knowledge, there has been no report of a 3c-3e silane adduct. A substantial challenge in the stabilization of 3c-3e interactions is that one of the two species participating in the interaction is a radical, which can undergo further reaction with the 3c-3e adduct to generate two strong 2c-2e bonds (Figure 2C,D). Kinetic barriers for the reactions of radicals tend to be low, so that the low prevalence of 3c-3e interactions is readily accounted for by a decomposition pathway that is thermodynamically favorable, and, in the absence of steric or geometric restrictions, extremely facile. Ribas and coworkers reported a rare example of a 3c-3e adduct between a macrocycle-supported Cu(II) and a C–H bond on the ligand, which decomposes readily via a bimolecular pathway.²⁵ Wayland previously demonstrated that the extreme steric

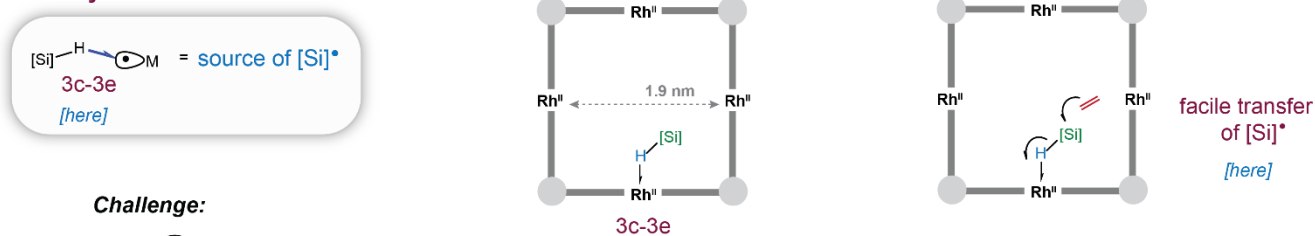
bulk surrounding Rh(II) in **2** permitted EPR observation of 3c-3e interactions with ethylene (Figure 2D).²⁶ Addition of ethylene to less sterically encumbered **1** leads to rapid addition of the metalloradicals across the ethylene double bond, likely via the intermediacy of a 3c-3e ethylene adduct of **1** (Figure 2C). Even for bulky **2**, the 3c-3e adduct only proved stable at low temperature, and irreversible insertion of two ethylene molecules between a pair of Rh(II) porphyrin complexes was observed upon heating (Figure 2D). Prior work on Rh(II) porphyrin systems highlights four salient points: i) spin density from the rhodium center is partially shifted to the carbon center of the ethylene 3c-3e adduct; ii) this spin density can be used to form substrate-substrate bonds (Figure 2D) but iii) if sterically accessible, formation of substrate-catalyst bonds is preferred (Figure 2C) and iv) even if substrate-substrate bond formation occurs, two Rh(II) metalloradicals are converted into unreactive carbon ligated Rh(III) centers (Figure 2D). To stabilize a 3c-3e σ -adduct of a metalloradical, follow-up reactions with

another metalloradical thus need to be prevented. Here we show that thermally stable 3c-3e adducts can be generated via geometric frustration. Rh(II) porphyrins that are site-isolated in a MOF matrix are not sterically encumbered and thus able to form σ -complexes with weakly donating silanes. The geometric frustration of Rh(II) sites in the MOF ensures that the σ -adduct cannot be approached by another metalloradical to furnish undesired closed-shell dimers (Figure 2B). The resulting stability of the 3c-3e adduct permits the assembly of tri-component transition state for direct silyl radical transfer with an activation barrier of 20 kcal \cdot mol⁻¹ (Figure 1D). An alternative pathway that proceeds via free silyl radicals is associated with a minimum energy barrier of \sim 35 kcal \cdot mol⁻¹ and was realized experimentally with the assistance of 390 nm photons, which carry an energy of 73 kcal \cdot mol⁻¹. Both direct silyl transfer and release of free silyl radicals can be achieved from the 3c-3e σ -adduct, so that the relative facility of both pathways could be directly compared.

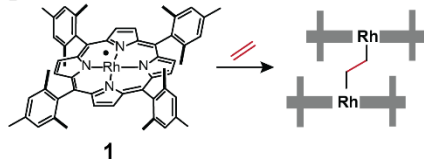
A Silylium Transfer



B Silyl Radical Transfer



C



D

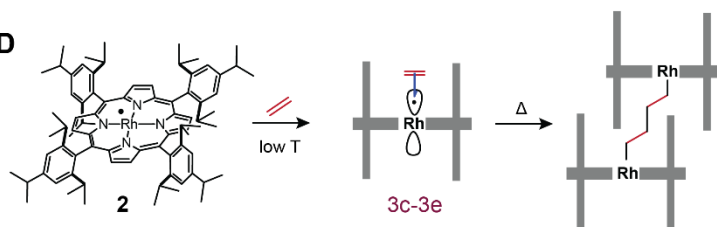


Figure 2. A 3c-2e interactions between transition metals activates silanes towards the transfer of silylium equivalents while (B) the 3c-3e interaction present in the MOF-supported Rh(II)-silane adduct activates silanes towards silyl radical transfer. In solution, 3c-3e adducts can readily react with another metal center with an unpaired spin to furnish two 2c-2e bonds in a fast and favorable cleavage of the 3c-3e adduct. Moderate (C) or substantial (D) steric bulk does not prevent 2c-2e bond formation for homogeneous catalysts. The half-arrow notation introduced by Green and Parkin for 3-center bonding is used throughout this work.²⁷

RESULTS AND DISCUSSION

We have previously shown that Rh(II) centers site-isolated in the porphyrin-containing MOFs PCN-224 (Rh(II)-**3**) or PCN-222 (Rh(II)-**4**) are efficient hydrosilylation catalysts.²⁸ Comparison with homogeneous model systems established

that heterogenization substantially benefited both the catalyst's activity and selectivity. In this work, we set out to elucidate the origin of the reactivity differences that emerge when Rh(II) porphyrin centers are placed in a MOF-environment. Prior to in-depth mechanistic studies, we excluded that hydrosilylation proceeded via a radical chain reaction initiated by Rh(II) based on the following evidence:

(i) prior literature reports state that trialkylsilanes are unsuitable substrates for hydrosilylation via a radical chain mechanism,²⁹ (ii) no reaction was observed when we replaced **3** with AIBN (Figure S1–S3), and (iii) an on-off experiment showed substantial differences in the reaction rate in the presence and absence of light (Figure S4). The active Rh(II) catalyst is generated by photolysis of a Rh(III)-Me pre-catalyst during which methyl radicals are generated. We could exclude that methyl radicals contribute noticeably to the observed reactivity since no decrease in reaction rates was observed when re-used catalyst (from which no

methyl radicals can be released) was used to catalyze olefin hydrosilylation (Figure S5–S6). Based on detailed EPR analyses, labeling and trapping experiments, kinetic data, as well as solution and solid-state NMR experiments, which we will discuss below, we propose the catalytic cycles depicted in Figure 3, which are corroborated by quantum-chemical calculations. Our proposal includes two different reaction pathways for the rate-limiting transfer of silyl radical from the silane to the olefin, of which one leads to the generation of free silyl radicals, while the second pathway achieves a direct silyl radical transfer to the olefin.

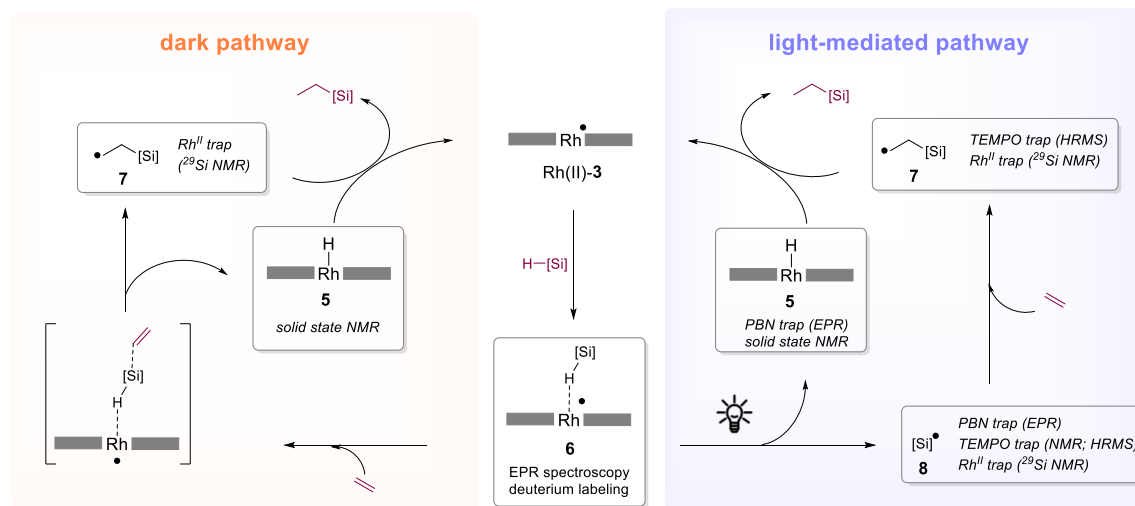


Figure 3. Proposed reaction mechanism that comprises distinct pathways available in the absence (left) and presence (right) of light ($\lambda = 390$ nm). Each intermediate is labeled with the experimental evidence that supports its presence.

Characterization of the active catalyst

While we have previously shown that photolysis of Rh(Me)-**3** gave rise to reactivity that was consistent with the formation of site-isolated Rh(II), no direct evidence for the formation of Rh(II) was provided. Here we present direct characterization of Rh(II)-**3** and Rh(II)-**4** via continuous-wave (CW) EPR spectroscopy (Figure 6A). The shape of the EPR signal arises from the coupling of the electronic spin $S=1/2$ of Rh(II) with the nuclear spin of ^{103}Rh $I=1/2$ with $g_{\perp} > g_{\parallel}$ typical of a d_{z^2} singly occupied molecular orbital (SOMO). Computer simulations of the spectrum shows the contribution of a major species with spin Hamiltonian parameters consistent with the reported data for homogeneous porphyrin Rh(II) metalloradicals in a frozen solvent matrix (Figure S23 and S32).³⁰ We also derived the average distance between Rh(II) centers in Rh(II)-**3** and Rh(II)-**4** from line shape analysis of the EPR spectra. By assuming that the broadening of EPR signals results from the interaction between adjacent Rh(II) centers and applying a simple dipolar coupling model (Figure S32 and Table S12), we obtained Rh(II)-Rh(II) intermolecular separation values of 1.81 nm in the case of Rh(II)-**3** and 1.24 nm for Rh(II)-**4**. Both values are in good agreement with the separation between porphyrin centers in the X-ray structures of PCN-224 (1.9 nm) and PCN-222 (1.06 nm for triangular pores).^{31–35} A larger discrepancy is expected for PCN-222 due to the presence of hexagonal as well as triangular pores, so that the dipolar coupling observed by EPR is averaged over two sets of

Rh(II) centers located at different distances. The agreement between EPR-derived Rh(II)-Rh(II) separations and the crystallographically determined porphyrin spacing is consistent with a complete conversion of Rh(III)Me to Rh(II) sites upon irradiation. Complete conversion of Rh(III)-Me to Rh(II) was further confirmed by ^1H -NMR analysis of the metalloporphyrin linker that was recovered when Rh(II)-**3** or Rh(II)-**4** were subjected to digestion under basic conditions.²⁸ We also observed the presence of methane and toluene after Rh(Me)-**3** was irradiated in benzene, which is consistent with the release of methyl radicals that undergo reaction with the benzene solvent, as previously described by Wayland and co-workers.³⁶ Notably, EDX analysis of **3** recovered from catalytic reactions remained consistent with the complete metalation of all porphyrin sites by rhodium.²⁸

To confirm that the metalloradical species, Rh(II)-**3**, observed by EPR spectroscopy constitutes a kinetically competent catalyst for olefin hydrosilylation, we monitored the rate of ethylene hydrosilylation (Figure 4). Direct use of Rh(Me)-**3** in light-promoted hydrosilylation showed an initiation period of close to 5 h, which we attribute to the conversion of the bench-stable Rh(III)-Me precursor to catalytically active Rh(II)-**3** (Figure 4A). Since site-isolation renders the Rh(II) catalyst stable to storage under inert conditions, direct use of Rh(II)-**3** in catalysis could also be tested (Figure 4B). As expected, the initiation period disappeared for Rh(II)-**3**, and the effective rate constant is identical within experimental error to that observed with Rh(Me)-**3**

after 5 h of reaction (Figure 4A). Rh(II)-3 is thus gradually formed under the light-mediated reaction conditions and is a kinetically competent catalyst for olefin hydrosilylation.

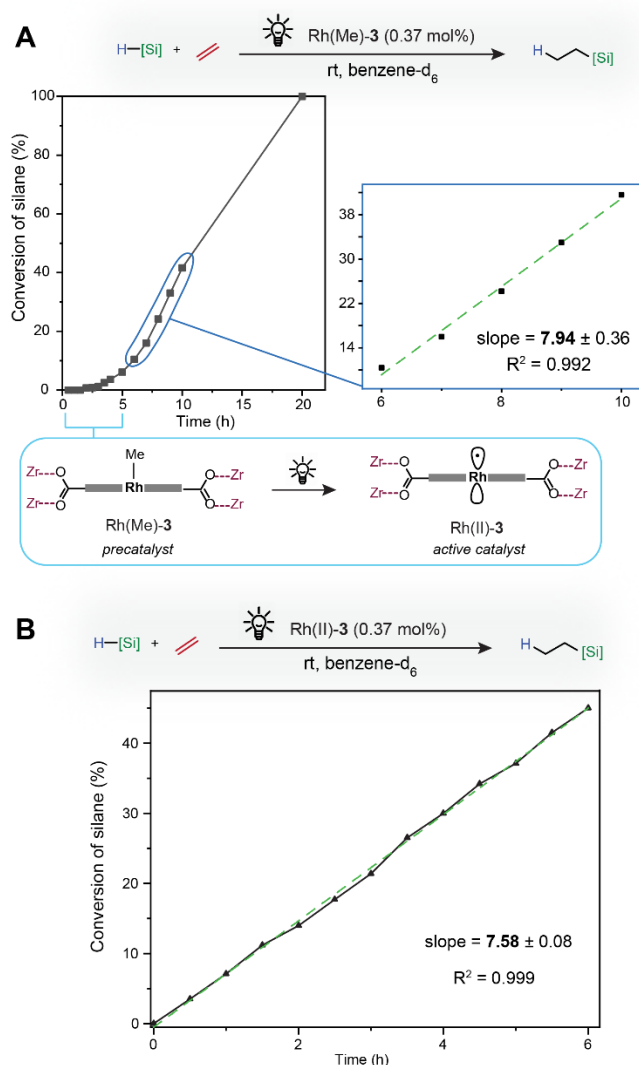


Figure 4. Silane conversion over time in the light-mediated hydrosilylation of ethylene with the Rh(Me)-3 precatalyst (A) and with isolated Rh(II)-3 (B).

Oxygen Effect on Thermal Hydrosilylation

In order to compare the kinetic profile of light-mediated and thermal hydrosilylation with Rh(II)-3, we attempted numerous in-situ NMR experiments. Unfortunately, duplicate measurements frequently gave rise to notably different conversion rates (Figure S8–S10). During our search for the source of the rate variation, we employed increasingly rigorous means of excluding oxygen during the synthesis of active catalyst Rh(II)-3. When the reaction was set up in an argon-filled glove box with freeze-pump-thaw deoxygenated benzene we obtained Rh(II)-3 that gave rise to only 4% conversion in hydrosilylation. Metalloradical Rh(II)-3 is itself an effective oxygen trap, so we recycled the benzene for subsequent syntheses of the active catalyst. Rh(II)-3 from the first recycle achieved 2% conversion and Rh(II)-3 from the second recycle gave only 0.3% conversion, compared to

~20% conversion for Rh(II)-3 prepared with benzene that was only sparged with argon. To test whether the addition of small amounts of oxygen during the preparation of Rh(II)-3 increased the catalyst's hydrosilylation performance, we introduced controlled amounts of air (Figure 5A,B). Two plateaus were observed that corresponded to the addition of ~1 equivalent of O₂ and more than 10 equivalents of O₂ per Rh(II) center, respectively. While addition of 10 – 33 equivalents of O₂ furnished Rh(II)-3 that was able to achieve close to 50% conversion, Rh(II)-3 that was prepared in air was substantially less active (Figure 5B). We confirmed that oxygen rather than any other components of non-dried air was responsible for the rate enhancement by repeating key experiments with dried O₂ gas (Figure S17).

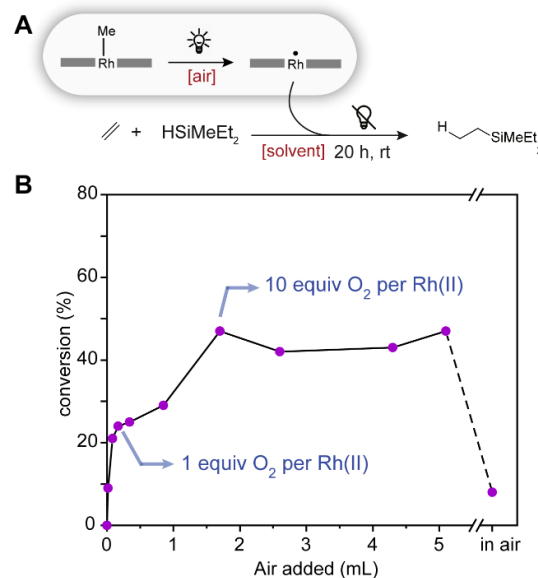


Figure 5. A Evaluation of the effect of oxygen during active catalyst preparation in benzene (B) and the effect of the solvent on the performance of Rh(II)-3 in thermal hydrosilylation (room temperature, 20 h unless stated otherwise).

In a series of control experiments (Figure S14–S15), we determined that i) while O₂ must be present during active catalyst formation, the presence of O₂ during the use of Rh(II)-3 in hydrosilylation is detrimental, and that ii) O₂ and light must be present simultaneously. We knew from prior EPR experiments that the exposure of Rh(II) to air in the absence of light furnished Rh(III)-superoxide **9**. We confirmed that superoxide formation is reversible in the presence of light, and Rh(II)-3 could be quantitatively recovered after 20 h of illumination (Figure S18). Furthermore, Rh(III)-superoxide **9** was unable to promote olefin hydrosilylation. While Rh(III)-superoxide formation was not directly responsible for the beneficial effect of O₂, we speculated that **9** may be converted into Rh(III)-hydroperoxide **10** in the presence of both light and O₂. A light-promoted HAT from the benzene solvent to **9** would give rise to **10** and phenyl radicals during the preparation of the active catalyst. In support of such a pathway, mass spectrometric analysis of the reaction solvent led to the detection of biphenyl-h₁₀ when Rh(II)-3 formation was carried out in benzene and biphenyl-d₁₀ when benzene-d₆ was used as a solvent (Figure S20–S21). Fur-

thermore, FTIR analysis of Rh(II)-**3** generated in the presence of 10 equivalents of O₂ furnished a band at 829 cm⁻¹ which is in good agreement with an O–O stretch of 823 cm⁻¹ for a reported rhodium-hydroperoxide (Figure S22).³⁷ The band in question was absent for Rh(II)-**3** generated in air-free solvent and increased in intensity when 50 equivalents of O₂ were present during Rh(II)-**3** formation. We thus propose that diamagnetic Rh(III)-hydroperoxide **10** is formed alongside Rh(II)-**3** when the active catalyst was prepared in the presence of a limited amount of O₂. The beneficial effect of the converting a small number of Rh(II) centers to polar Rh(III)-O–OH groups raised the possibility that ethylene hydrosilylation may occur via a polar transition state, which is explored in detail in later sections. For consistency with our earlier work, kinetic experiments and experimental activation barriers presented in the later part of this work were determined for an oxygen content that corresponds to the first plateau in Figure 5B. EPR spectroscopic characterization of reaction intermediates presented in the main text refer to rigorously deoxygenated samples in order to minimize the signal intensity of **9**. However, all spectroscopic observations were also carried out for samples with varying oxygen content to verify that all intermediates discussed below (but no additional intermediates) were likewise generated in the presence of oxygen (see SI for detailed discussion).

Characterization of the silane σ -adduct

After ensuring that Rh(II) metalloradicals, the catalytically active centers in hydrosilylation, can be quantitatively generated throughout the MOF framework, we studied the interaction between the Rh(II) center with reagents: Addition of diethylmethylsilane to a suspension of Rh(II)-**3** gave rise to an immediate and drastic change in the appearance of the EPR spectrum, which was consistent with the formation of 3c-3e silane σ -adduct **6**. The EPR signal of **6** is associated with substantially different g -values compared to Rh(II)-**3**, which can be rationalized based on the bonding interactions predicted by first principle quantum mechanical calculations of **6**. The increase in the electron density at the Rh center brought about by σ -donation from the silane to the Rh center lifts the energy of the d_{z^2} orbital and thus increases the energy gap between the d_{z^2} and d_{xz}/d_{yz} orbitals. Since $g_{\perp} = g_e + \frac{6\lambda}{\Delta E_{z^2 \leftarrow xz,yz}}$ (where λ is the spin-orbit coupling constant and $\Delta E_{z^2 \leftarrow xz,yz}$ is the energy gap between the d_{z^2} and d_{xz}/d_{yz} orbitals) a lower g_{\perp} value is expected for **6** than for Rh(II)-**3**.^{38, 39} Theoretical calculations located an energy minimum for an η^1 σ -adduct that features a 146° Rh–H–Si angle (Figure 6C). In theoretical calculations, a Gibbs energy of $\Delta G_{\text{calc}} = -3.1$ kcal·mol⁻¹ was obtained for σ -adduct **6**, along with predicted EPR parameters that are in good agreement with experimental observation (Figure 6B, Table S7). The Si–H bond is only slightly elongated in **6** (1.56 Å) compared to the Si–H bond in the free silane (1.51 Å), and back-donation from the Rh(II) SOMO to the Si–H σ^* orbital makes only a minimal contribution to the Rh–silane interaction in **6** (Table S16). Theoretical calculations also predicted a maximum hyperfine splitting of about 48 MHz due to the H atom that bridges the Rh and Si centers. Unfortunately, the spectral features expected due to the coupling to ¹H were not

fully resolved in the spectrum and generated only a broadening of the EPR signal around $g = 1.980$.

To verify experimentally that the 3c-3e silane σ -adduct adopts an η^1 coordination mode, **6**, and its deuterated variant D-**6**, (Figure 6D) were interrogated by hyperfine sublevel correlation spectroscopy (HYSCORE).⁴⁰ The predicted ¹H hyperfine coupling for the H atom bridging Si and Rh atoms was outside the detection range of HYSCORE experiments at Q-band frequency. However, the gyromagnetic ratio of deuterium, which is about 7 times smaller than that of ¹H, rendered the ²H hyperfine interaction measurable. The Q-band HYSCORE spectra recorded at a magnetic field corresponding to the g_x of both **6** and D-**6** exhibit a complex pattern at low frequency in both the (–,+) and (+,+) quadrants due to the interaction of the unpaired electron with ¹⁴N nuclei ($I=1$) from the porphyrin ring. The correlation peaks are further split into multiplets due to the quadrupole interaction. Therefore single-quantum and nominally forbidden double-quantum transitions are observed in the spectra (Figure S30–S31). While the HYSCORE spectrum of **6** was characterized only by the presence of ¹⁴N signals, the spectrum of D-**6** also shows cross-peaks centered at the ²H Larmor frequency ($\nu_L = 6.7$ MHz) separated by approximately 7 MHz. Measured ²H hyperfine coupling constants are in good agreement with values calculated (Table S11) for the structural model proposed for **6** (Figure 6C). EPR spectroscopy could also furnish direct evidence for the light-mediated cleavage of silane σ -adduct **6**. While **6** was still observed when a sample of it was stored at room temperature for 20 h, subjecting an identical sample to irradiation (390 nm) for 30 minutes led to the disappearance of the signal attributable to **6** (Figure 6E). Crucially, no Rh(II) signal was observed after irradiation, which is consistent with the silane σ -adduct undergoing HAT, but not with dissociation of **6** into Rh(II) and silane. Theoretical calculations support that HAT from the silane to Rh(II) in the absence of an additional interaction with ethylene is thermally inaccessible at room temperature ($\Delta G_{\text{calc}}^{\ddagger} = 39.1$ kcal·mol⁻¹), but silyl radical release from **6** becomes thermodynamically feasible in the presence of light (the energy of a 390 nm photon corresponds to 73.3 kcal·mol⁻¹; see Figures S63 and S69 for detailed discussion). In particular, many of the bright states of **6** were predicted to have significant charge transfer character from the SOMO, which is localized on the Rh–H–Si 3c-3e bond, to the porphyrin ligand (Figure S63–S64). The SOMO has bonding character for Si–H and anti-bonding character for Rh–H, so that excitation of one electron from the SOMO weakens the Si–H bond but strengthens the Rh–H bond. Light excitation thus facilitates Si–H bond cleavage, despite the fact that the Si–H bond (BDFE = 28.7 kcal·mol⁻¹) is substantially stronger than the Rh–H bond (BDFE = 3.1 kcal·mol⁻¹) in the ground state.

Notably, however, EPR spectroscopy also provided evidence for the presence of an additional thermally accessible pathway: addition of ethylene led to the disappearance of 3c-3e silane adduct **6** within 20 h at room temperature (Figure 6E). The absence of signals attributable to Rh(II)-**3** or its ethylene complex supported the proposal that ethylene addition led to hydrosilylation along with formation of diamagnetic Rh(III)–H. To understand the interactions of

Rh(II)-**3** with ethylene and silanes in more detail, we introduced ethylene to a benzene suspension of Rh(II)-**3**, which resulted in the formation of 3c-3e π -adduct **11**. Our assignment was based on the excellent agreement of the spectral features of **11** with those reported by Wayland and coworkers

for the ethylene 3c-3e π -adduct generated from sterically shielded Rh(II) porphyrin **2**.³⁸ Next, we exposed active catalyst Rh(II)-**3** dispersed in benzene to both silane and ethylene in the absence of light and immediately froze the EPR sample in liquid nitrogen.

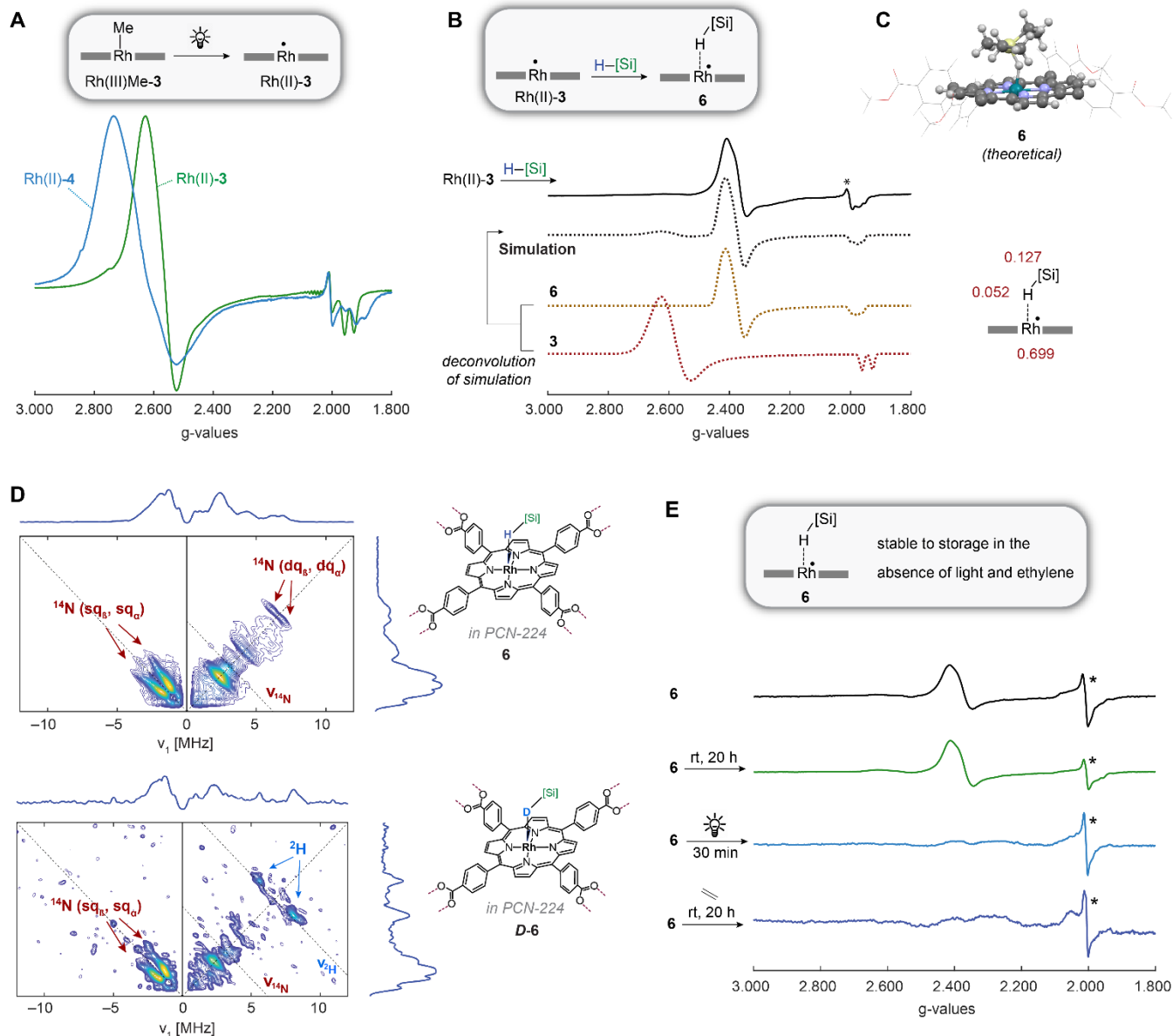


Figure 6. **A** X-band EPR spectra of Rh(II) metalloradicals site isolated in PCN-224 (Rh(II)-**3**) or PCN-222 (Rh(II)-**4**) measured at 77 K. **B** Experimental and simulated X-band EPR spectrum of Rh(II)-**3** after exposure to silane measured at 77 K (calculated structure of **6** that was used in the simulation along with calculated spin populations depicted on the right). **C** Theoretical calculated structure of **6** obtained with the ORCA program package⁴¹ at the BP86-D3/SARC-ZORA-TZVP(Rh)/ZORA-def2-TZVP(Si)/ZORA-def2-SVP(C,H,O,N) level. **D** Q-band HSCORE spectra recorded at 8 K at the magnetic field corresponding to g_x position of the HSiEt₃ (top) and the DSiEt₃ (bottom) σ -adducts of Rh(II) site-isolated in PCN-224. **E** EPR spectra of **6** that was either stored in the dark for 20 h, exposed to light for 30 min or exposed to ethylene in the dark for 20 h. Features marked with an asterisk were assigned to porphyrin-centered radical centers present within the metal-free PCN-224 seeds used in the MOF synthesis in accordance with previous literature reports.^{42, 43}

The resulting sample contained a new species associated with $g_x = 2.322(5)$, $g_y = 2.233(5)$ and $g_z = 1.984(3)$, in addition to ethylene adduct **11** and silane adduct **6**. We subsequently confirmed that the new signal was detected irrespective of the order in which ethylene and silane were

added to Rh(II)-**3** (Figure 7A,B). Having ruled out addition complexes of oxygen, water, or benzene solvent (Table S9), we considered that the signal may originate from van der Waals adduct **12** or bis-axial adduct **13** (Figure 7C). Theoretical calculations estimated a value of 2–4 MHz for the

coupling between the unpaired spin and the ethylene protons in **13** (Table S8). However, the low signal-to-noise ratio of the echo-detected signal at $g = 2.322$ position prevented experimental verification of the presence of weak coupling interactions. Theoretical calculations predicted, however, that the association of ethylene in adduct **12** is only fleeting (Figure S58), so that spectroscopic observation of **12** was deemed unlikely. We thus tentatively attribute the signal with $g_x = 2.322$, which was only observed when both ethylene and silane were present, to the formation of **13** (Table S8). Since we had found that the addition of larger amounts of O_2 during the formation of Rh(II)-**3** led to an increased activity of the active catalyst during hydrosilylation, we tested whether the increased catalytic activity was associated with the formation of any new radical intermediates.

However, no new species were observed by EPR spectroscopy when Rh(II)-**3** was generated in the presence of ~ 10 instead of ~ 1 equivalents of O_2 , either for the active catalyst itself or in the presence of added reagents (Figure S28–S29). The intensities of the signals corresponding to Rh(II)-**3**, **6**, and **13** decreased with an increase in the amount of O_2 present during Rh(Me)-**3** photolysis, however, due to competing formation of Rh(III)-superoxide **9**. For a sample of Rh(Me)-**3** that was subjected to photolysis under air, all Rh(II)-derived EPR signals were barely detectable, and only 6% conversion was achieved in thermal ethylene hydrosilylation (Figure 5B and S29). The observation of a sharp decrease in catalyst activity when Rh(II)-**3** was generated in air is consistent with Rh(II) centers directly participating in the assembly of the transition state structure.

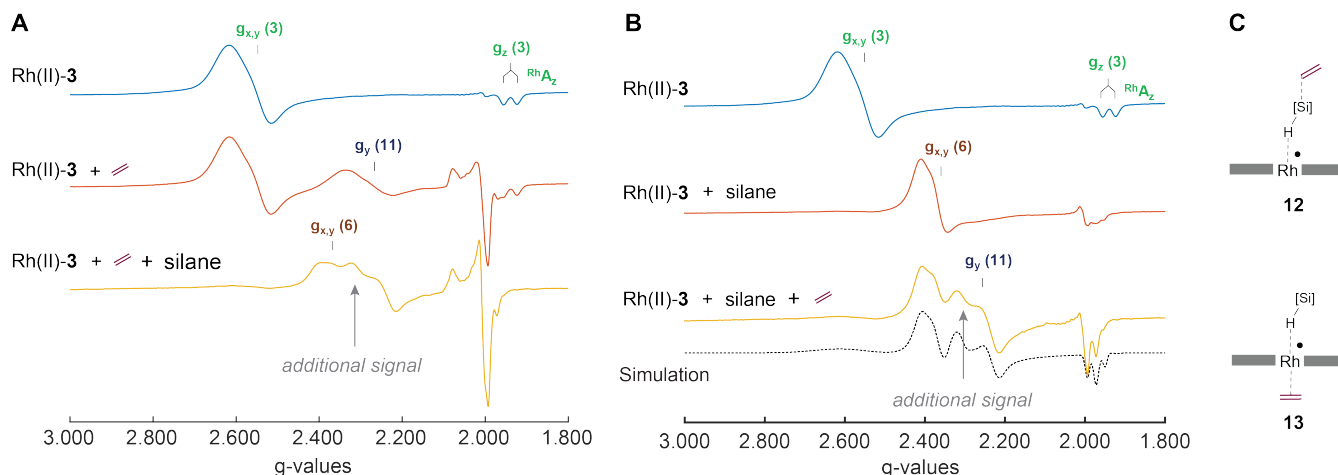


Figure 7. X-band EPR spectra measured at 93 K of Rh(II)-**3** in benzene to which (A) first ethylene and then silane was added and (B) first silane and then ethylene was added. C Proposed structures for the intermediate that gave rise to a signal at $g_x = 2.322(5)$, which is indicated in A and B with grey arrows.

Detection of Radical Intermediates

After analysis of the interaction of reagents with the Rh(II) center we turned our attention to the detection of the proposed reaction intermediates. Since σ -adduct **6** is a stable species in the absence of light and ethylene, silyl radical **8** was only an expected intermediate for the light-mediated hydrosilylation mechanism, while the formation of carbon-centered radical **7** was expected for both dark and the light-mediated reaction pathway (Figure 3). Indeed, addition of 1 equivalent of TEMPO to the light-mediated hydrosilylation reaction permitted the trapping of both suspected key intermediates, **7** and **8**, as **16** and **17** (Figure 8D and S33–S34).²⁸ TEMPO trapping experiments rely on the capture of fleeting radicals by a persistent radical. A persistent radical that is always present under the reaction conditions is Rh(II)-**3**, so we wondered if Rh(II) could be used directly as a radical trap, which would minimize the perturbation of the system. A particular concern was that TEMPO may not only be able to capture free silyl radical **8**, but potentially also abstract a silyl radical equivalent from **6** (Figure S37–S40). Reliance on Rh(II) as a radical trap has the advantage that Rh(II) centers remain immobilized within the MOF framework and are unable to approach **6**, while free silyl radical **8** could re-

act with Rh(II) centers. Only a very minor portion of the organic radicals could potentially undergo radical-radical recombination with Rh(II) (an irreversible process under thermal conditions), because efficient thermal turnover of the Rh(II) catalyst was observed. To enable a sufficient amount of radical trapping products to accumulate to permit detection, we thus carried out Rh(II)-catalyzed thermal hydrosilylation for two days before the MOF was recovered and analyzed by solid-state ^{29}Si NMR spectroscopy. A signal for **15**, the product expected for the trapping of **7** by Rh(II), and to a lesser extent also **14**, the trapping product of **8** by Rh(II), could be observed (Figure 8A). An approximate quantification is possible via comparison of the intensity of the signals of **15** and **14** with the signal at 7.7 ppm (marked with an asterisk in Figure 8A), which we attribute to node-bound silanol species. Silanol was formed as minor ($\sim 0.5\%$) by-product in all hydrosilylation reactions. The exact amount of silanol observed depends on the level of water and oxygen contamination of the hydrosilylation reaction (Figure S41–S42). The chemical shift observed for the additional peak in Figure 8A is consistent with both Zr-O-SiMeEt_2 and $\text{Et}_2\text{MeSi-O-SiMeEt}_2$, but because the species in question was not removed by washing of the MOF prior to NMR analysis, we tentatively assign the peak to silanol interacting with the MOF nodes of **3**. Since a silanol-derived

signal constituted the most intense feature in the solid-state ^{29}Si NMR spectra of recovered catalysts, only a minute fraction of the silicon-centered and carbon-centered radicals were trapped by Rh(II) centers in the MOF.

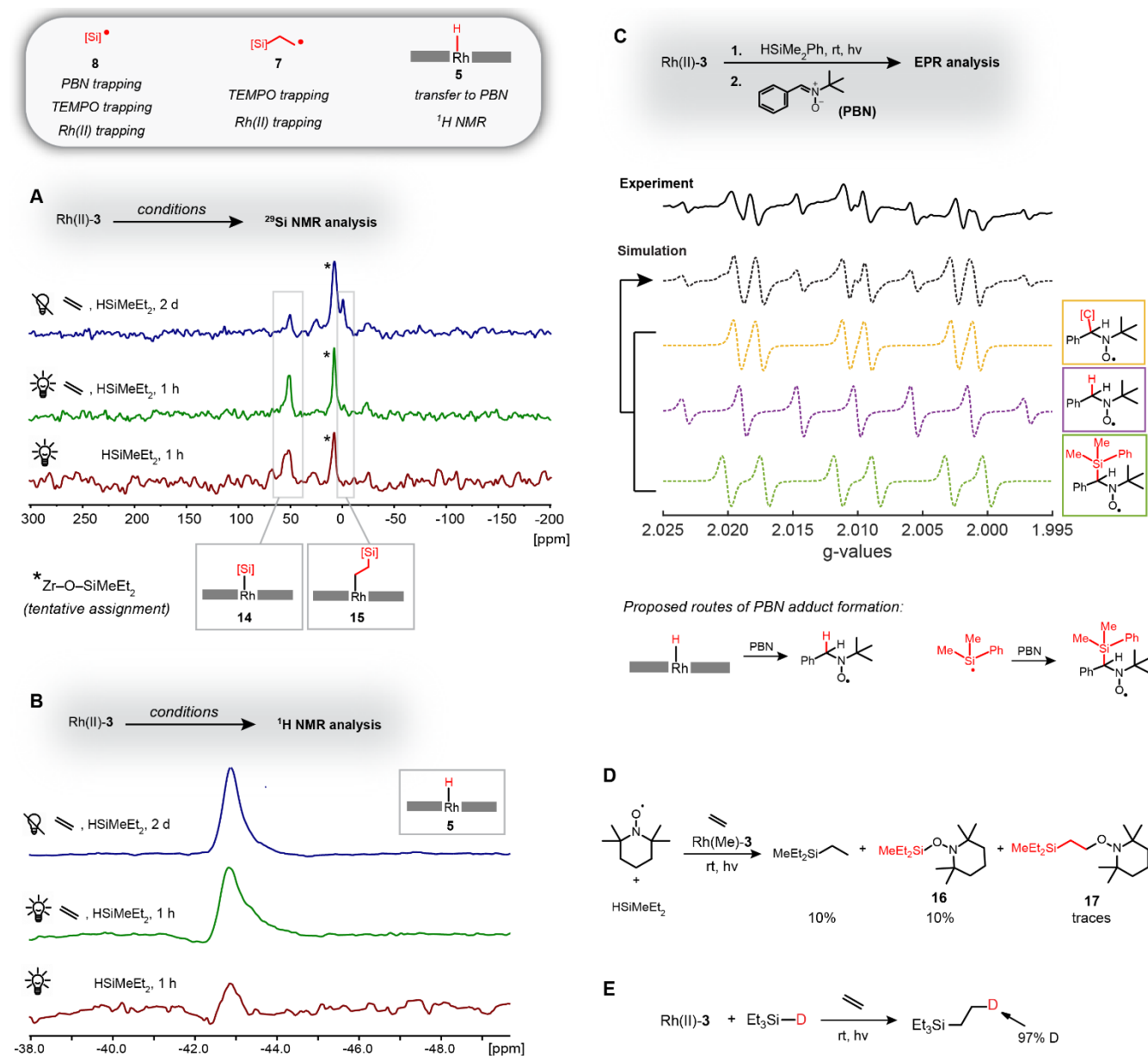


Figure 8. Experimentally observed reaction intermediates. **(A)** ^{29}Si $\{^1\text{H}\}$ CP MAS NMR spectra of **14** and **15** generated as off-cycle intermediates via radical-radical recombination of silicon- and carbon-centered radicals with Rh(II)-3. **(B)** Solid state ^1H -NMR spectra of **5** generated by exposure of Rh(II)-3 to silane (and ethylene) in the presence or absence of light. **(C)** EPR data obtained when Rh(II)-3-catalyzed hydrosilylation reaction was carried out in the presence of PBN along with the proposed route of formation for the PBN adducts that were observed by EPR. **(D)** Addition of TEMPO to hydrosilylation catalyzed by Rh(II)-3.²⁸ **(E)** Deuterium originally attached to silane reagent is efficiently incorporated into hydrosilylation product.

Because the detection of Rh-[Si] **14** alongside Rh-CH₂-CH₂-[Si] **15** in catalyst retrieved from thermal hydrosilylation was surprising, further comparative experiments were carried to evaluate a potential contribution of silyl radicals to thermal hydrosilylation. Addition of **8** to Rh(II) could be discerned by solid-state ^{29}Si NMR analysis of recovered **3** from light-mediated hydrosilylation (**14** in Figure 8A). When Rh(III)Me-3 was irradiated in the presence of only silane,

Rh-[Si] **14** could again be detected (Figure 8A), which substantiates that light-mediated silyl radical release from **6** was possible even in the absence of olefin. For both experiments under light-mediated reaction conditions, a reaction time of 1 h led to the accumulation of a larger amount of Rh-[Si] **14** than was observed in thermal hydrosilylation after 2 d, even though the formation of the Rh-[Si] bond in **14** is reversible in the presence of light. Solid-state NMR data

thus indicated that the concentration of silyl radicals is substantially smaller under thermal conditions versus photochemical conditions. Trapping of carbon-centered radical **7**, on the other hand, was only observed for thermal hydrosilylation. To gain further insight into the reaction condition-dependent contribution of silyl radicals, we performed double-label experiments with DSiEt_3 and HSiMeEt_2 (Figure S43). Analysis of residual silane after a reaction time of 23 h in the absence of light furnished a $\text{Et}_3\text{SiD} : \text{Et}_2\text{MeSiD}$ ratio of 4.5 : 1, while a 1 : 1 ratio was observed for photochemical conditions. Since a 1:1 ratio of Et_3SiD and Et_2MeSiD was already established after a reaction time of only 0.5 h in light-mediated hydrosilylation, we could conclude that H/D exchange proceeded very efficiently in the presence of silyl radicals. The limited H/D exchange observed under thermal reaction conditions thus indicates that silyl radicals are only formed in minute amounts under thermal hydrosilylation conditions while direct formation of **7** constitutes the dominant pathway in the dark.

Irrespective of whether **7** is formed directly from **6** (thermal pathway), or whether hydrosilylation proceeds via light-promoted expulsion of **8** from **6** (photochemical pathway), however, Rh(III)-H (**5**) was expected to constitute a key reaction intermediate in both pathways. The ability of C-centered radicals to abstract a hydrogen atom from H-Rh(III) porphyrin complexes was shown already in 1985 by Halpern and coworkers.⁴⁴ Rh(III)-H could therefore undergo hydrogen atom abstraction by a carbon-based radical to yield the hydrosilylation product and regenerate Rh(II) . We thus set out to gather evidence for the formation of Rh(III)-H under both light-mediated and dark reaction conditions. Solid-state $^1\text{H-NMR}$ analysis of **3** recovered for hydrosilylation reactions under light-promoted or dark conditions both furnished a signal at -43 ppm, which indicates the presence of a hydride ligand trans to a vacant coordination site (Figure 8B).²¹ To provide an unambiguous assignment we also prepared a Rh(III)-H complex derived from the homogeneous model system **18** for the MOF catalyst, the $^1\text{H-NMR}$ signal of which was in good agreement with that obtained from recovered **3** (Figure S44). We could furthermore show that Rh(III)-H **5** was also formed in the absence of ethylene, so that light-mediated release of silyl radical **8** from **6** is a viable reaction step in light-mediated olefin hydrosilylation. To obtain additional evidence that the proposed intermediated **5** and silyl radical **8** are formed under the reaction conditions, we performed EPR spectroscopy after addition of the spin trap *N-tert-butyl- α -phenylnitrone* (PBN; Figure 8C). The formation of three different radical intermediates could be detected upon irradiation of a mixture of Rh(II)-3 and HSiMe_2Ph . Based on the respective hyperfine coupling constants of the ^1H nucleus in the α position, we could conclude that PBN adducts of carbon-, silicon- and hydrogen-centered radicals contribute to the experimentally observed signal. A previous report of successful transfer of a hydrogen atom from Au-H to PBN substantiates our assignment that the hydrogen atom trapped by PBN originated from **5**.⁴⁵ To confirm that a PBN adduct of a silyl radical contributed to the experimentally observed signal we repeated the experiment with HSiEt_3 (Figure S48), whereupon we observed noticeable changes in the EPR

spectrum due to small differences in the Si hyperfine coupling with HSiMe_2Ph versus HSiEt_3 .⁴⁶⁻⁴⁸

Molecular Dynamics Simulations

Formation of carbon-centered radical intermediate **7**, either via addition of **8** to ethylene or direct silyl transfer, is expected to be irreversible: Quantum mechanical calculations show that intermediate **7** is stabilized by $\Delta G_{\text{calc}} = 15.8$ kcal·mol⁻¹ relative to **8** and ethylene. We propose that **7** undergoes HAT with Rh(III)-H **5** to reform Rh(II)-3 . Use of deuterated silane confirmed that the deuterium atom originally present in the silane was fully transferred to the hydrosilylation product (Figure 8E). Molecular dynamics simulations (GFN2-xTB with certain semiempirical parameters re-fitted against DFT data; see Figure S66) were able to provide additional insight into the fate of key intermediate **7**. Monitoring the evolution of **7** within the MOF pore over a period of 50 ps showed that more than 72% of the carbon-centered radicals were converted into the hydrosilylation product via HAT with Rh(III)-H . Interestingly, as our model contained only one Rh(III)-H bond, the observed product is exclusively formed from **7** that did not escape its solvent cage and reacted with “its own” Rh center. Only 8% of **7** left the solvent cage and thus could potentially undergo HAT with other Rh(III)-H bonds or be trapped by Rh(II) (Fig. S67). The H and Si atoms present in the hydrosilylation product therefore predominantly originate from the same silane precursor molecule. As anticipated, ethylene expulsion from **7** to yield **8** was not observed, so that we attribute the silyl radical **8** observed experimentally as originating from bimolecular HAT. Half of the remaining 20% of **7** underwent addition to the porphyrin linker (Figure S67). Circumstantial experimental evidence that a small fraction of the radicals generated may undergo addition to the porphyrin ligand could be obtained from radical trapping experiments with PBN (Figure 8C). Specifically, trapping of a carbon centered radical was also observed for experiments in which only silane but no ethylene was present, so that the carbon-centered radical that was trapped could not be **7**. Instead, a porphyrin-based radical formed upon addition of **8** to the porphyrin linker may account for the carbon centered radical trapped by PBN. Alternatively, PBN could have undergone reaction with methyl radicals generated from residual Rh(Me)-3 that was still present in the Rh(II)-3 sample. Digestion of Rh(II)-3 followed by solution $^1\text{H-NMR}$ analysis did not reveal the presence of any remaining Rh(III)-Me . However, considering the higher sensitivity of EPR compared to NMR, we cannot rule out that the carbon-based radical trapped by PBN corresponds to methyl radicals derived from Rh(Me)-3 impurities in Rh(II)-3 . EPR analysis of recovered catalyst samples also repeatedly showed peaks of varying intensity with $g = 2$, which could indicate the presence of a porphyrin centered radical or a Rh superoxo species.⁴⁹ While prior EPR studies of porphyrin-containing MOFs have attributed similar features to porphyrin centered radicals,^{42,50} we also observed the presence of the signal in question for **3** which had never been subjected to hydrosilylation catalysis (Figure 6E). Considering all available data, we conclude that radical addition to the porphyrin linker may take place, but we cannot comment to the extent or reversibility of this process. Should the porphyrin linker

in **3** undergo derivatization, however, it does not appear to affect its catalytic performance, at least within the first 8 uses of the catalyst.

Assistance by Adjacent Rh Center

While we had gathered various pieces of experimental evidence that the presence of ethylene enables H–Si bond cleavage at room temperature, a transition state model constructed based on the existing data delivered an unrealistically high calculated Gibbs energy of activation (Figure 9A). Considering that thermal hydrosilylation with Rh(II)-**3** can occur at room temperature, it cannot be associated with Gibbs energy of activation that substantially exceeds ~ 20 kcal·mol⁻¹. Numerous alternative proposed transition structures also furnished unrealistically high activation barriers or could not be located by our computational approach (Figure S55). Since initial models only considered one isolated Rh(II) porphyrin center, we considered that the discrepancy may arise from the promotional effects of the extended environment. Interestingly, when a second Rh(II) porphyrin center was positioned at the distance set by the MOF framework, an electron transfer from the Rh–H–Si–ethylene adduct to the adjacent Rh(II) center could take place. Electron transfer gave rise to a zwitterionic transition state (Figure 9B) that was slightly lower in energy than the neutral transition state (Figure 9A). Prior EPR studies had shown however that simultaneous addition of silane and ethylene to Rh(II)-**3** led to the formation of bis-adduct **13** (Figure 7). Trans-ligation of Rh by an electron-donating ligand would be expected to stabilize the cationic Rh center present in a zwitterionic transition state (Figure 9B) and thus lower the barrier associated with it. Theoretical models indicated that, while an ethylene adduct is accessible, it is 4.7 kcal·mol⁻¹ less stable than a benzene adduct of **6**. However, the increased electron donation provided by ethylene compared to benzene as the trans ligand on Rh(II) led to superior stabilization of the transiently positively charged transition structure. Even taking into account the estimated energy penalty of 4.7 kcal·mol⁻¹ for the formation of **13**, the transition state structure depicted in Figure 9D gave rise to the lowest barrier observed thus far (29.7 kcal·mol⁻¹). Interestingly, intrinsic reaction coordinate (IRC) analysis showed that the electron transfer from the ethylene adduct of **13** to an adjacent Rh(II) center occurs immediately prior to the transition state (Figure 9C). Shortly after the barrier is crossed, a second electron transfer takes place which returns both Rh centers to an oxidation state of two (Figure S62). While the theoretical model now accounted for the promotional effect of an adjacent rhodium center, it did not reproduce the polarity of the extended environment. Since computation of an entire MOF pore at even the DFT level with a double zeta basis set was too expensive, we accounted for the higher polarity of the MOF pore environment versus a benzene solvent environment via a correction to the dielectric constant in the solvent model (Table S23). Use of a dielectric constant consistent with the calculated polarizability of the MOF, as well as complete filling of the MOF's pores by benzene, furnished a theoretical Gibbs energy of activation of 24.9 kcal·mol⁻¹.

While the theoretical model clearly highlighted the beneficial effect of a second Rh(II) center in close proximity to the active site, the computed reaction pathway was not yet consistent with a transformation that could take place at room temperature. Notably, however, the theoretical model does not account for the presence of Rh(III)-O–OH within the MOF pore. While the beneficial effect of the presence of these polar groups could be clearly established experimentally, their absolute concentration or spatial distribution is not known, which precluded inclusion in the theoretical model. Importantly, however, a number of experimentally testable hypotheses result from the lowest energy pathway provided by theoretical calculations: i) the involvement of ethylene in the highest energy transition state suggests that thermal hydrosilylation is associated with an ethylene order of at least 1, likely even 2 (if ethylene serves as the trans ligand on Rh(II) as depicted in Figure 9D), ii) a polar solvent environment would be expected to stabilize the partial charges created in the transition state of the thermal hydrosilylation reaction, and iii) the amount of dehydrosilylated side product obtained would be expected to be higher for the thermal pathway due to the possibility of facile proton loss from the zwitterionic transition structure.

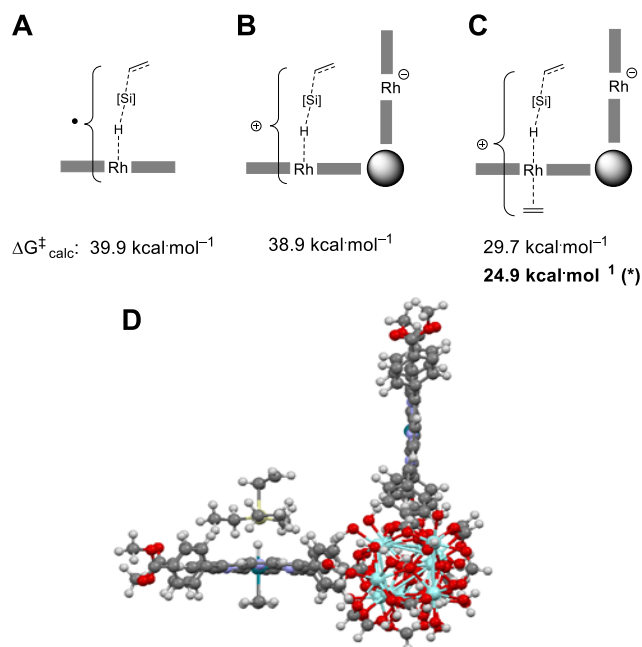


Figure 9. (A–C) Potential transition state structures along with the Gibbs energy of activation obtained for them with the ORCA program package⁴¹ at the DLPNO-CCSD(T)/SARC-ZORA-TZVP(Rh)/ZORA-def2-TZVP(C,H,O,N,Si) // BP86-D3/SARC-ZORA-TZVP(Rh)/ZORA-def2-TZVP(Si)/ZORA-def2-SVP(C,H,O,N) level. *Polarity of MOF environment considered in calculation. (D) Theoretical model of the transition state structure (corresponds to model 9C).

We had shown in our earlier work that thermal conditions led to a hydrosilylation selectivity of 92% whereas light-mediated conditions were associated with a selectivity of 99%. The light-mediated pathway, which proceeds via free silyl radicals, is substantially faster at room temperature than the thermal pathway, which proceeds by direct silyl transfer via a zwitterionic transition. The selectivity of a light-

mediated reaction at room temperature is thus expected to be dominated by the selectivity associated with the silyl radical reaction pathway. When the photochemical reaction is carried out at 50 °C, the contribution of the thermal pathway becomes substantial and the selectivity for the formation of the hydrosilylated product drops to 93%. The formation of an increased amount of hydrosilylated product whenever the thermal reaction pathway is a dominant contributor to the reaction rate is consistent with the zwitterionic transition state depicted in Figure 9C. We also investigated the origin of the substantially lower selectivity observed in light-mediated hydrosilylation with the molecular analogue of Rh(III)-**3**, the results of which are discussed in the Supporting Information (Figure S70).

Kinetic Isotope Effect

To assess whether kinetic analysis of ethylene hydrosilylation would shed light on the rate determining transition state or would instead be overshadowed by mass transport limitations, we determined the kinetic isotope effect. The formation of the σ -adduct, which is the only step preceding Si-H cleavage, is not associated with any notable weakening of the Si-H bond and therefore does not show a significant equilibrium isotope effect.⁵¹ Consequently, the experimental kinetic isotope effect (KIE) could be determined by direct competition of HSiEt₃ and DSiEt₃, which ensures higher accuracy for a heterogeneous (light-mediated) reaction than would be possible for the comparison of absolute rate constants.⁵² Determination of the H:D ratios for tetraethylsilane formed in the presence of both HSiEt₃ and DSiEt₃ furnished a KIE of 1.85 ± 0.24 for light-mediated hydrosilylation and 1.90 ± 0.25 for thermal hydrosilylation with Rh(II)-**3** (Table S24–S25). The KIE was identical within experimental error for the light-mediated and the dark reaction. A KIE of 1.9 ± 0.25 substantiated that Si-H cleavage takes place in the turnover limiting step, which is the case for both reaction pathways we have outlined. Furthermore, the experimental kinetic isotope effect is in excellent agreement with the theoretically predicted value of 1.9 for the dark reaction (Figure S69). Notably, because the experimental intermolecular KIE is not substantially lowered compared with theoretical predictions, mass transfer of the silane through the MOF pore network is not limiting the reaction rate.⁵³

Reaction Orders and Eyring Analysis

During kinetic investigations of thermal olefin hydrosilylation we had to rely on analysis of reaction aliquots because mass transfer limitations were observed when thermal hydrosilylation was carried out inside an NMR tube. Interestingly, even the dissolution of ethylene could become substantially inhibited within narrow vessels. In-situ monitoring of ethylene hydrosilylation reaction catalyzed by Rh(II)-**3** led to an abrupt cessation of conversion once the ~0.6 equivalents of ethylene initially dissolved in the reaction solvent were converted, despite the availability of additional ethylene in the headspace of the NMR tube (Figure S11). We could confirm ethylene dissolution limitations by EPR, were the concentration of **13** detected was strongly dependent on the extent to which EPR tubes were shaken

(Figure S12). Determination of reaction orders was thus carried out in standard reaction vials from which aliquots were repeatedly collected for NMR analysis. A change in the olefin substrate from ethylene to 1-pentene was deemed necessary to prevent escape of ethylene during sampling. A catalyst reaction order of one, as well as a silane reaction order of 1.3 could be determined by reaction progress kinetic analysis via graphical overlay developed by Blackmond and Bures (Figure S74–S81).^{54–56} Reaction order analysis for 1-pentene led to a value of 0.7, but due to the larger variability within data sets collected for 1-pentene, we could only conclude that the 1-pentene order was non-zero and likely ~1 (Figure S82–S84). The reaction orders determined are consistent with a rate-limiting transition state that involves Rh(II)-**3**, silane, as well as olefin. Notably, theoretical calculations suggest that the coordination of an electron-donating substituent such as ethylene or silane in the trans position of the Rh(II) porphyrin leads to a substantial reduction in calculated Gibbs energy of activation. Based on EPR observation of intermediate **13**, ethylene was used as an exemplary ligand for all theoretical analyses. However, the experimentally determined 1-pentene order of ~1 excluded 1-pentene coordination in the trans position of Rh(II) during 1-pentene hydrosilylation. We suspect that the increased steric bulk of 1-pentene compared to ethylene could disfavor π -coordination of 1-pentene, so that silane likely occupies the axial coordination site on Rh(II). A silane order of 1.3 is consistent with the participation of more than one silane molecule in the generation of transition state, and theoretical calculations indicate that occupation of the trans position on Rh(II) by silane instead of benzene solvent reduces the reaction barrier by 7.4 kcal·mol⁻¹ (Table S21). The slower hydrosilylation rate observed with 1-pentene versus ethylene is consistent with reduced stabilization of a zwitterionic transition structure due to the less efficient electron-donation from a silane compared to an ethylene ligand to Rh(II).

Since the replacement of ethylene with a non-gaseous olefin led to noticeable reduction in the reaction rate, we determined the experimental Gibbs energy of activation for the hydrosilylation of ethylene itself to permit comparison between experimental and computational data. It was practically challenging to obtain temperature dependent kinetic data for a reaction that requires a solid catalyst, liquid as well as gaseous reagents, and for which the oxygen concentration has a substantial effect on the reaction rate, so that the quality of the data obtained was only modest (Table S29–31). Nonetheless, experimental activation parameters of $\Delta G^\ddagger_{\text{exp}}$ (298 K) = 19.4 ± 0.6 kcal·mol⁻¹, and $\Delta H^\ddagger_{\text{exp}}$ = 17.6 ± 2.7 kcal·mol⁻¹ could be extracted from an Eyring analysis (Table S32–33, see section 21.2 in SI). To consider the possibility that ethylene may serve as the trans ligand for Rh(II) in ethylene hydrosilylation, we calculated $\Delta G^\ddagger_{\text{exp}}$ both for an olefin order of 1 (the experimentally determined value for 1-pentene) as well as 2 (based on the theoretical proposal for ethylene), which led to values of $\Delta G^\ddagger_{\text{exp}}$ = 20.0 kcal·mol⁻¹ (ethylene order = 1) and $\Delta G^\ddagger_{\text{exp}}$ = 18.8 kcal·mol⁻¹ (ethylene order = 2), respectively. Consequently, even the upper end of the error range for $\Delta G^\ddagger_{\text{exp}}$ is substantially below the minimum barrier required to promote hydrosilylation via silyl

radical intermediates. It must be stated, however, that direct comparison of the numerical values for the barriers does not provide immediate information on the practical feasibility of the two reaction pathways due to a difference in reaction orders. Unlike the rate of olefin hydrosilylation via the intermediacy of silyl radicals, which would not be expected to depend on the olefin concentration, direct silyl transfer to olefins has a non-zero olefin order, so that low concentrations of olefin could lead to a low reaction rate even for low values of $\Delta G^\ddagger_{\text{exp}}$.

Solvent Effect

Based on the mechanism proposed for direct silyl radical transfer, a rate acceleration would be expected when the polarity of the solvent is increased: Electron transfer from the adjacent porphyrin center leads to the generation of charges in the transition state, so that a polar solvent environment would be expected to stabilize the transition structure. To ensure that any observed rate differences were not caused by varying ethylene concentrations in solution, we selected a number of solvents for which the experimentally determined ethylene solubility fell into a narrow range (Table S42).⁵⁷ For *n*-hexane, benzene, chlorobenzene, and hexafluoroisopropanol (HFIP), the total amount of ethylene present during experiments corresponded to 2.2 – 2.5 equivalents relative to silane, of which 0.5 – 0.8 equiv were present in solution. Hexane, which showed the highest ethylene solubility but has the lowest dielectric constant ($\epsilon = 1.88$),⁵⁷ gave rise to slower silane conversion (Figure 10). On the other hand, replacement of benzene with HFIP ($\epsilon = 16.7$) increased the conversion to above 80% after a reaction time of 20 h. We also examined ethylene hydrosilylation in HFIP with Rh(II)-3 prepared in the presence of 1 mL of air: complete conversion was observed after 20 h, and even after 5 h, a conversion of 32% had already been reached (Figure 10). We attribute the rate enhancement to the formation of a larger number of Rh(III)-O-OH sites that may provide internal solvation to polar transition structures assembled on adjacent Rh(II) centers. The observation of a pronounced oxygen effect in a polar solvent such as HFIP suggests that solvent molecules in the pore cannot fully compensate for the polar stabilization Rh(III)-O-OH moieties provide to the zwitterionic transition state.

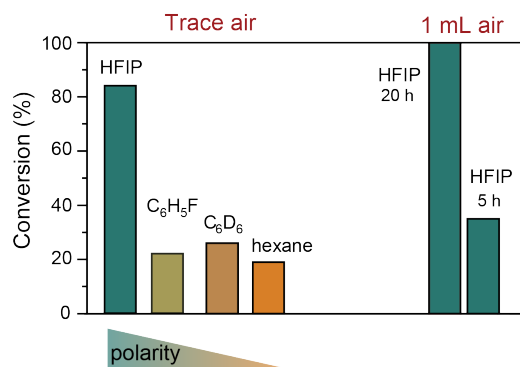


Figure 10. Solvent effect on thermal ethylene hydrosilylation catalyzed by Rh(II)-3 (room temperature, 20 h reaction time unless stated otherwise).

DISCUSSION

We embarked on a systematic study to understand why Rh(II) porphyrin centers site isolated in a MOF host were able to promote thermal hydrosilylation of olefins, whereas structurally analogous molecular catalysts proved unreactive. One potential challenge with the molecular catalyst is that the dimerization via Rh–Rh bond formation readily takes place, which depletes the concentration of Rh(II) porphyrin. Preserving a monomeric Rh(II) species in solution is insufficient, however, because no thermal hydrosilylation is observed either with **1**, which is sterically shielded from Rh–Rh bond formation. While steric bulk is effective for preventing Rh–Rh bond formation, it offers poor protection for 3c-3e adducts: Even the extreme steric protection offered by four 2,6-diisopropyl phenyl substituents was only able to stabilize a porphyrin Rh(II)-ethylene 3c-3e adduct at low temperatures. The geometric protection offered by the MOF matrix permits the formation of a 3c-3e ethylene π -adduct, and even a 3c-3e silane σ -adduct that both remain stable at room temperature. The combination of stability and steric accessibility of the novel 3c-3e silane σ -adduct **6** permits it to engage with other reaction partners, such as olefins. Pre-assembly of silane and Rh(II) to form **6** renders it entropically feasible to assemble a tri-component transition state in which the C–Si bond is formed in concert with formation of the Rh–H bond and cleavage of the H–Si bond. For a molecular complex in solution, a corresponding tri-component transition state is entropically inaccessible because no 3c-3e silane σ -adduct adduct can be generated. Site-isolation alone is however insufficient to enable facile direct silyl radical transfer: We found that an electron transfer that takes place as the system approaches the transition state is necessary to enable olefin hydrosilylation to take place at room temperature. While isolated Rh(II) centers could potentially be obtained by attachment of suitably functionalized Rh(II) porphyrin molecules to a support surface, the high degree of spatial organization provided by the MOF host is crucial for ensuring that a Rh(II) center is sufficiently close to a transition structure to engage in facile electron transfer. Additionally, we also found evidence for an unexpected stabilization of the transition structure due to the formation of Rh(III)-O-OH during photolysis of the Rh(Me) precatalyst. Small amounts of O₂ exert a pronounced beneficial effect on thermal ethylene hydrosilylation, which we rationalized by considering that the co-generation of minor amounts of Rh(III)-O-OH alongside Rh(II) would position polar groups in close spatial proximity to the active site. The promotional effect of Rh(III)-O-OH remained pronounced when benzene was replaced by HFIP as the reaction solvent, which suggests the effect of proximally located Rh(III)-O-OH is not trivial to recreate via variation of the solvent environment. Notably, both the observation of substantial rate increases in the presence of a polar solvent, and an increase in the formation of the dehydrosilylated reaction products support that electron transfer from an adjacent rhodium center occurs during thermal hydrosilylation.

In an attempt to quantify the beneficial effect that the MOF host imparts on olefin hydrosilylation catalysis, we considered the minimum energy pathways that would enable hy-

drosilylation to take place in the absence of MOF-specific effects. In solution, **18** rapidly generates **19**, **20** and **21** (Figure 11), and the Rh–Si BDFE for **21** was computationally estimated to be 67.4 kcal·mol⁻¹. A thermal cleavage to generate silyl radicals which could engage in hydrosilylation is consequently not feasible. Next, we considered a system containing site-isolated Rh(II) centers which could stabilize a 3c-3e silane σ -adducts. H–Si cleavage to release silyl radical would be thermodynamically accessible ($\Delta G_{\text{calc}} = 28.7$ kcal·mol⁻¹), but kinetically inaccessible due to the entropic contribution to the activation barrier which results in $\Delta G^{\ddagger}_{\text{calc}} = 39.1$ kcal·mol⁻¹. Furthermore, cleavage of the weak Rh–H bond ($\Delta G_{\text{calc}} = 3.1$ kcal·mol⁻¹) in σ -adduct **6** to re-form Rh(II) and silane would be expected to take place in preference to silyl radical formation. Lastly, a direct transfer pathway, analogous to the one observed within the MOF host, is associated with $\Delta G^{\ddagger}_{\text{calc}} = 39.9$ kcal·mol⁻¹ if no proximally located electron acceptor is available. The MOF platform thus permitted not only the stabilization of a highly unusual 3c-3e σ -adduct, but also enabled a formal silyl radical transfer at room temperature that leverages the spatial organization of Rh(II) centers in the framework. An experimental activation barrier of $\Delta G^{\ddagger}_{\text{exp}} = 19.4 \pm 0.6$ kcal·mol⁻¹ was determined for Rh(II)-3-catalyzed ethylene hydrosilylation in benzene, which is substantially lower than the barriers associated with both observed and hypothetical reaction pathways outside the MOF.

Molecular Analogue of Rh(II)-3

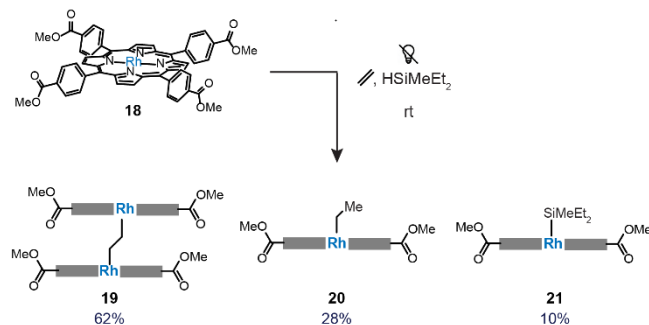


Figure 11. Complex **18**, a molecular analogue of Rh(II)-3 does not catalyze thermal hydrosilylation.

CONCLUSION

We have shown that olefin hydrosilylation catalyzed by site isolated Rh(II) metalloradicals **3** or **4** can proceed via two pathways, both of which involve 3c-3e silane σ -adduct **6**. In the presence of light, free silyl radicals are generated from **6**, which subsequently add to olefins. H-atom transfer between the resulting carbon-centered radical and Rh(III)-H regenerates the active Rh(II) catalyst. In the absence of light, however, σ -adduct **6** is stable at room temperature both in the dry state and when suspended in benzene. Intermediate **6** pre-organizes Rh(II) and silane for participation in a tri-component transition structure with olefins that permits facile thermal hydrosilylation. By synchronizing Rh–H bond formation, H–Si bond cleavage and Si–C bond formation, the direct silyl transfer pathway limits the number of high-energy intermediates that need to be formed over the course of the reaction. The MOF-based catalyst,

which has access to a direct silyl transfer pathway from intermediate **6** can thus promote hydrosilylation at room temperature, while a molecular analogue which was unable to stabilize a 3c-3e silane σ -adduct furnished negligible amounts of product even at 140 °C.

AUTHOR INFORMATION

#These authors contributed equally.

ORCID:

0000-0003-1004-1140 (C.N.N.)

0000-0002-2070-836X (P.C.B.)

0000-0002-4540-8734 (Z.W.)

0000-0002-8628-6497 (Z.Q.)

Corresponding Author

*neumann@kofo.mpg.de

*alexander.schnegg@cec.mpg.de

Author Contributions

All data was collected and analyzed by Z.Q., P.C.B., Z.W., H. D., S.C., C.F. and M. L. with input from C.N.N., A.S. and F.N. The project was conceived by Z.Q. and C.N.N. and directed by C.N.N. and A.S. The initial draft of the manuscript was written by C.N.N. and all authors contributed to the editing process.

Funding Sources

Financial support was provided by the Lise-Meitner Program of the MPG, the Max-Planck Society, as well as by a Humboldt postdoc fellowship to Z.Q. and a CSC scholarship to H. D..

ACKNOWLEDGMENT

We thank the service departments of the Max-Planck-Institut für Kohlenforschung. The authors would like to thank Johnson Matthey plc for the award some of the platinum group metal materials used in this research, the CSC for a PhD scholarship to H.D., as well as the Alexander von Humboldt Gesellschaft for a postdoc fellowship to Z.Q..

ABBREVIATIONS

TEMPO, (2,2,6,6-Tetramethylpiperidin-1-yl)oxyl; AIBN, Azobisisobutyronitrile; PBN, N-tert-Butyl- α -phenylnitrone; KIE, kinetic isotope effect; HAT, hydrogen atom transfer.

REFERENCES

- Chan, A. Y.; Perry, I. B.; Bissonnette, N. B.; Buksh, B. F.; Edwards, G. A.; Frye, L. I.; Garry, O. L.; Lavagnino, M. N.; Li, B. X.; Liang, Y.; Mao, E.; Millet, A.; Oakley, J. V.; Reed, N. L.; Sakai, H. A.; Seath, C. P.; MacMillan, D. W. C., Metallaphotoredox: The Merger of Photoredox and Transition Metal Catalysis. *Chem. Rev.* **2022**, 122 (2), 1485-1542 doi: 10.1021/acs.chemrev.1c00383.
- Schultz, D. M.; Yoon, T. P., Solar Synthesis: Prospects in Visible Light Photocatalysis. *Science* **2014**, 343 (6174), 1239176 doi: 10.1126/science.1239176.
- Palla, F.; Salpeter, E. E.; Stahler, S. W., Primordial star formation: The role of molecular hydrogen. *Astrophys. J.* **1983**, 267 (2), 632-641 doi: 10.1086/161231.
- Vallance, C., *An Introduction to Chemical Kinetics*. Morgan & Claypool Publishers: 2017; doi:10.1088/978-1-6817-4664-7.

5. Mirahmadi, M.; Pérez-Ríos, J., Three-body recombination in physical chemistry. *Int. Rev. Phys. Chem.* **2022**, *41* (3-4), 233-267 doi: 10.1080/0144235X.2023.2237300.
6. Ryu, H.; Park, J.; Kim, H. K.; Park, J. Y.; Kim, S.-T.; Baik, M.-H., Pitfalls in Computational Modeling of Chemical Reactions and How To Avoid Them. *Organometallics* **2018**, *37* (19), 3228-3239 doi: 10.1021/acs.organomet.8b00456.
7. Steinberg, I. Z.; Scheraga, H. A., Entropy Changes Accompanying Association Reactions of Proteins. *J. Biol. Chem.* **1963**, *238* (1), 172-181 doi: 10.1016/s0021-9258(19)83978-9.
8. Ryde, U., A fundamental view of enthalpy–entropy compensation. *Med. Chem. Commun.* **2014**, *5* (9), 1324-1336 doi: 10.1039/c4md00057a.
9. Luo, X. L.; Crabtree, R. H., Homogeneous catalysis of silane alcoholysis via nucleophilic attack by the alcohol on an Ir(η^2 -HSiR₃) intermediate catalyzed by [IrH₂S₂(PPh₃)₂]SbF₆ (S= solvent). *J. Am. Chem. Soc.* **1989**, *111* (7), 2527-2535 doi: 10.1021/ja00189a026.
10. Park, S.; Brookhart, M., Hydrosilylation of Carbonyl-Containing Substrates Catalyzed by an Electrophilic η^1 -Silane Iridium(III) Complex. *Organometallics* **2010**, *29* (22), 6057-6064 doi: 10.1021/om100818y.
11. Metsänen, T. T.; Hrobárik, P.; Klare, H. F.; Kaupp, M.; Oestreich, M., Insight into the Mechanism of Carbonyl Hydrosilylation Catalyzed by Brookhart's Cationic Iridium (III) Pincer Complex. *J. Am. Chem. Soc.* **2014**, *136* (19), 6912-6915 doi: 10.1021/ja503254f.
12. Jiang, H.-J.; Simon, H. D. A.; Irran, E.; Klare, H. F. T.; Oestreich, M., Experimental Mechanistic Analysis of Carbonyl Hydrosilylation Catalyzed by Abu-Omar's Rhenium(V) Oxo Complex. *Organometallics* **2023**, *42* (1), 48-54 doi: 10.1021/acs.organomet.2c00500.
13. Du, G.; Abu-Omar, M. M., Catalytic Hydrosilylation of Carbonyl Compounds with Cationic Oxorhenium(V) Salen. *Organometallics* **2006**, *25* (20), 4920-4923 doi: 10.1021/om060503z.
14. Matthews, S. L.; Pons, V.; Heinekey, D. M., Silane Complexes of Electrophilic Metal Centers. *Inorg. Chem.* **2006**, *45* (16), 6453-6459 doi: 10.1021/ic052134p.
15. Ríos, P.; Díez, J.; López-Serrano, J.; Rodríguez, A.; Conejero, S., Cationic Platinum(II) σ -SiH Complexes in Carbon Dioxide Hydrosilation. *Chem. Eur. J.* **2016**, *22* (47), 16791-16795 doi: 10.1002/chem.201603524.
16. Park, S.; Bézier, D.; Brookhart, M., An Efficient Iridium Catalyst for Reduction of Carbon Dioxide to Methane with Trialkylsilanes. *J. Am. Chem. Soc.* **2012**, *134* (28), 11404-11407 doi: 10.1021/ja305318c.
17. Yang, J.; Brookhart, M., Reduction of Alkyl Halides by Triethylsilane Based on a Cationic Iridium Bis(phosphinite) Pincer Catalyst: Scope, Selectivity and Mechanism. *Adv. Synth. Catal.* **2009**, *351* (1-2), 175-187 doi: 10.1002/adsc.200800528.
18. Yang, J.; Brookhart, M., Iridium-Catalyzed Reduction of Alkyl Halides by Triethylsilane. *J. Am. Chem. Soc.* **2007**, *129* (42), 12656-12657 doi: 10.1021/ja075725i.
19. Yang, J.; White, P. S.; Brookhart, M., Scope and Mechanism of the Iridium-Catalyzed Cleavage of Alkyl Ethers with Triethylsilane. *J. Am. Chem. Soc.* **2008**, *130* (51), 17509-17518 doi: 10.1021/ja806419h.
20. Hoyano, J.; Elder, M.; Graham, W. A., Hydrogen-bridged silicon-rhenium bonds. A diphenylsilane complex of rhenium carbonyl. *J. Am. Chem. Soc.* **1969**, *91* (16), 4568-4569 doi: 10.1021/ja01044a054.
21. Yang, J.; White, P. S.; Schauer, C. K.; Brookhart, M., Structural and Spectroscopic Characterization of an Unprecedented Cationic Transition-Metal η^1 -Silane Complex. *Angew. Chem. Int. Ed.* **2008**, *47* (22), 4141-4143 doi: 10.1002/anie.200705359.
22. Ríos, P.; Fouilloux, H.; Vidossich, P.; Díez, J.; Lledós, A.; Conejero, S., Isolation of a Cationic Platinum(II) σ -Silane Complex. *Angew. Chem. Int. Ed.* **2018**, *57* (12), 3217-3221 doi: 10.1002/anie.201712791.
23. Ríos, P.; Conejero, S.; Fernández, I., Bonding Situation of σ -E-H Complexes in Transition Metal and Main Group Compounds. *Chem. Eur. J.* **2022**, *28* (57), e202201920 doi: 10.1002/chem.202201920.
24. Scherer, W.; Meixner, P.; Barquera-Lozada, J. E.; Hauf, C.; Obenhuber, A.; Brück, A.; Wolstenholme, D. J.; Ruhland, K.; Leusser, D.; Stalke, D., A Unifying Bonding Concept for Metal Hydrosilane Complexes. *Angew. Chem. Int. Ed.* **2013**, *52* (23), 6092-6096 doi: 10.1002/anie.201210224.
25. Ribas, X.; Calle, C.; Poater, A.; Casitas, A.; Gómez, L.; Xifra, R.; Parella, T.; Benet-Buchholz, J.; Schweiger, A.; Mitrikas, G.; Solà, M.; Llobet, A.; Stack, T. D. P., Facile C-H Bond Cleavage via a Proton-Coupled Electron Transfer Involving a C-H...Cu^{II} Interaction. *J. Am. Chem. Soc.* **2010**, *132* (35), 12299-12306 doi: 10.1021/ja101599e.
26. Bunn, A. G.; Wayland, B. B., One-electron activation and coupling of ethene by rhodium(II) porphyrins: observation of an η^2 -ethene-metalloradical complex. *J. Am. Chem. Soc.* **1992**, *114* (17), 6917-6919 doi: 10.1021/ja00043a048.
27. Green, J. C.; Green, M. L. H.; Parkin, G., The occurrence and representation of three-centre two-electron bonds in covalent inorganic compounds. *Chem. Commun.* **2012**, *48* (94), 11481-11503 doi: 10.1039/C2CC35304K.
28. Qiu, Z.; Deng, H.; Neumann, C. N., Site-Isolated Rhodium(II) Metalloradicals Catalyze Olefin Hydrofunctionalization. *Angew. Chem. Int. Ed.* **2024**, *63* (18), e202401375 doi: 10.1002/anie.202401375.
29. Chatgililoglu, C., Structural and Chemical Properties of Silyl Radicals. *Chem. Rev.* **1995**, *95* (5), 1229-1251 doi: 10.1021/cr00037a005.
30. Sherry, A. E.; Wayland, B. B., Metalloradical activation of carbon monoxide. Formation and carbonyl coupling of a bent 17 electron M-CO unit. *J. Am. Chem. Soc.* **1989**, *111* (13), 5010-5012 doi: 10.1021/ja00195a081.
31. Gong, X.; Shu, Y.; Jiang, Z.; Lu, L.; Xu, X.; Wang, C.; Deng, H., Metal–Organic Frameworks for the Exploitation of Distance between Active Sites in Efficient Photocatalysis. *Angew. Chem. Int. Ed.* **2020**, *59* (13), 5326-5331 doi: 10.1002/anie.201915537.
32. Feng, D.; Chung, W.-C.; Wei, Z.; Gu, Z.-Y.; Jiang, H.-L.; Chen, Y.-P.; Darensbourg, D. J.; Zhou, H.-C., Construction of Ultrastable Porphyrin Zr Metal–Organic Frameworks through Linker Elimination. *J. Am. Chem. Soc.* **2013**, *135* (45), 17105-17110 doi: 10.1021/ja408084j.
33. Feng, D.; Gu, Z.-Y.; Li, J.-R.; Jiang, H.-L.; Wei, Z.; Zhou, H.-C., Zirconium-Metalloporphyrin PCN-222: Mesoporous Metal–Organic Frameworks with Ultrahigh Stability as Biomimetic Catalysts. *Angew. Chem. Int. Ed.* **2012**, *51* (41), 10307-10310 doi: 10.1002/anie.201204475.
34. Szczepkowska, A. M.; Janeta, M.; Siczek, M.; Tylus, W.; Trzeciak, A. M.; Bury, W., Immobilization of Rh(I) precursor in a porphyrin metal–organic framework – turning on the

- catalytic activity. *Dalton Trans.* **2021**, 50 (26), 9051-9058 doi: 10.1039/D1DT00518A.
35. Gallagher, A. T.; Malliakas, C. D.; Harris, T. D., CO Binding at a Four-Coordinate Cobaltous Porphyrin Site in a Metal–Organic Framework: Structural, EPR, and Gas Adsorption Analysis. *Inorg. Chem.* **2017**, 56 (8), 4654-4661 doi: 10.1021/acs.inorgchem.7b00292.
 36. Cui, W.; Zhang, X. P.; Wayland, B. B., Bimetallo-Radical Carbon–Hydrogen Bond Activation of Methanol and Methane. *J. Am. Chem. Soc.* **2003**, 125 (17), 4994-4995 doi: 10.1021/ja034494m.
 37. Carmona, D.; Lamata, M. P.; Ferrer, J.; Modrego, J.; Perales, M.; Lahoz, F. J.; Atencio, R.; Oro, L. A., Synthesis, characterization and molecular structure of the hydroperoxo complex $[(\eta^5\text{-C}_5\text{Me}_5)\text{Ir}(\mu\text{-pz})_3\text{Rh}(\text{OOH})(\text{dppe})][\text{BF}_4]$; Hpz = pyrazole, dppe = 1,2-bis(diphenylphosphino)ethane. *J. Chem. Soc., Chem. Commun.* **1994**, (5), 575-576 doi: 10.1039/C39940000575.
 38. Wayland, B. B.; Sherry, A. E.; Bunn, A. G., EPR studies of 1:1 complexes of rhodium(II) and cobalt(II) porphyrins with σ -donor and π -acceptor ligands: origins of rhodium(II) metalloradical reactivity. *J. Am. Chem. Soc.* **1993**, 115 (17), 7675-7684 doi: 10.1021/ja00070a011.
 39. McGarvey, B. R., Theory of the Spin Hamiltonian Parameters for Low Spin Cobalt(II) Complexes. *Can. J. Chem.* **1975**, 53 (16), 2498-2511 doi: 10.1139/v75-355.
 40. Höfer, P.; Grupp, A.; Nebenführ, H.; Mehring, M., Hyperfine sublevel correlation (hyscore) spectroscopy: a 2D ESR investigation of the squaric acid radical. *Chem. Phys. Lett.* **1986**, 132 (3), 279-282 doi: 10.1016/0009-2614(86)80124-5.
 41. Neese, F., Software update: The ORCA program system—Version 5.0. *Wiley Interdiscip. Rev. Comput. Mol. Sci.* **2022**, 12 (5), e1606 doi: 10.1002/wcms.1606.
 42. Lan, M.; Zhao, H.; Yuan, H.; Jiang, C.; Zuo, S.; Jiang, Y., Absorption and EPR spectra of some porphyrins and metalloporphyrins. *Dyes Pigm.* **2007**, 74 (2), 357-362 doi: 10.1016/j.dyepig.2006.02.018.
 43. Ren, Q.-Z.; Huang, J.-W.; Zhu, Z.-A.; Ji, L.-N.; Chen, Y.-T., Spectroscopic properties of p/p and o/o type iron(III)-metal-free porphyrin dimers and their catalysis as Cytochrome P450 model. *J. Porphyrins Phthalocyanines* **2001**, 5 (5), 449-455 doi: 10.1002/jpp.337.
 44. Paonessa, R. S.; Thomas, N. C.; Halpern, J., Insertion and oxidative addition reactions of rhodium porphyrin complexes. Novel free radical chain mechanisms. *J. Am. Chem. Soc.* **1985**, 107 (14), 4333-4335 doi: 10.1021/ja00300a044.
 45. Conte, M.; Miyamura, H.; Kobayashi, S.; Chechik, V., Spin Trapping of Au–H Intermediate in the Alcohol Oxidation by Supported and Unsupported Gold Catalysts. *J. Am. Chem. Soc.* **2009**, 131 (20), 7189-7196 doi: 10.1021/ja809883c.
 46. Tehfe, M.-A.; Lalevée, J.; Morlet-Savary, F.; Graff, B.; Blanchard, N.; Fouassier, J.-P., Tunable Organophotocatalysts for Polymerization Reactions Under Visible Lights. *Macromolecules* **2012**, 45 (4), 1746-1752 doi: 10.1021/ma300050n.
 47. Tehfe, M.-A.; Lalevée, J.; Morlet-Savary, F.; Graff, B.; Fouassier, J.-P., A Breakthrough toward Long Wavelength Cationic Photopolymerization: Initiating Systems Based on Violanthrone Derivatives and Silyl Radicals. *Macromolecules* **2011**, 44 (21), 8374-8379 doi: 10.1021/ma2017265.
 48. Qrareya, H.; Dondi, D.; Ravelli, D.; Fagnoni, M., Decatungstate-Photocatalyzed Si–H/C–H Activation in Silyl Hydrides: Hydrosilylation of Electron-Poor Alkenes. *ChemCatChem* **2015**, 7 (20), 3350-3357 doi: 10.1002/cctc.201500562.
 49. Sayari, A., Formation and stability of superoxide ions in Rh-zeolite catalysts. *React. Kinet. Catal. Lett.* **1989**, 39 (1), 155-161 doi: 10.1007/BF02061870.
 50. Feng, D.; Jiang, H.-L.; Chen, Y.-P.; Gu, Z.-Y.; Wei, Z.; Zhou, H.-C., Metal–Organic Frameworks Based on Previously Unknown Zr₈/Hf₈ Cubic Clusters. *Inorg. Chem.* **2013**, 52 (21), 12661-12667 doi: 10.1021/ic4018536.
 51. Churchill, D. G.; Janak, K. E.; Wittenberg, J. S.; Parkin, G., Normal and Inverse Primary Kinetic Deuterium Isotope Effects for C–H Bond Reductive Elimination and Oxidative Addition Reactions of Molybdenocene and Tungstenocene Complexes: Evidence for Benzene σ -Complex Intermediates. *J. Am. Chem. Soc.* **2003**, 125 (5), 1403-1420 doi: 10.1021/ja027670k.
 52. Simmons, E. M.; Hartwig, J. F., On the Interpretation of Deuterium Kinetic Isotope Effects in C–H Bond Functionalizations by Transition-Metal Complexes. *Angew. Chem. Int. Ed.* **2012**, 51 (13), 3066-3072 doi: 10.1002/anie.201107334.
 53. Wang, C.-H.; Gao, W.-Y.; Powers, D. C., Measuring and Modulating Substrate Confinement during Nitrogen-Atom Transfer in a Ru₂-Based Metal-Organic Framework. *J. Am. Chem. Soc.* **2019**, 141 (49), 19203-19207 doi: 10.1021/jacs.9b09620.
 54. Nielsen, C. D. T.; Burés, J., Visual kinetic analysis. *Chem. Sci.* **2019**, 10 (2), 348-353 doi: 10.1039/C8SC04698K.
 55. Burés, J., Variable Time Normalization Analysis: General Graphical Elucidation of Reaction Orders from Concentration Profiles. *Angew. Chem. Int. Ed.* **2016**, 55 (52), 16084-16087 doi: 10.1002/anie.201609757.
 56. Blackmond, D. G., Reaction Progress Kinetic Analysis: A Powerful Methodology for Mechanistic Studies of Complex Catalytic Reactions. *Angew. Chem. Int. Ed.* **2005**, 44 (28), 4302-4320 doi: 10.1002/anie.200462544.
 57. Sahgal, A.; La, H. M.; Hayduk, W., Solubility of ethylene in several polar and non-polar solvents. *Can. J. Chem. Eng.* **2009**, 56 (3), 354-357 doi: 10.1002/cjce.5450560313.

